A Multicomponent and Multiphase Model of Reactive Wetting

W. Villanueva[*], W.J. Boettinger[†], G.B. McFadden[‡], and J.A. Warren[†]

[*] Physics Department, Royal Institute of Technology, Stockholm, SE-10691 Sweden

[†] Metallurgy Division, National Institute of Standards and Technology, Gaithersburg, MD 20899, USA

[‡] Mathematical and Computational Sciences Division, National Institute of Standards and Technology,

Gaithersburg, MD 20899, USA

walterv@kth.se, william.boettinger@nist.gov, geoffrey.mcfadden@nist.gov, and james.warren@nist.gov

Keywords: Reactive wetting, intermetallic formation, multicomponent and multiphase model, Navier-Stokes flow

Abstract

A diffuse-interface model of reactive wetting with intermetallic formation is presented. The model incorporates fluid flow, solute diffusion, and phase change that are based on the total molar Gibbs energy of a ternary system with four phases. Numerical simulations were performed successfully revealing the complex behavior of the reactive wetting process that include nucleation and growth of an intermetallic phase, and initial rapid spreading followed by a slow and progressive spreading. In addition, the nucleation and growth of the intermetallic phase is shown to be directly influenced by its kinetic coefficient or the interface energy associated with it.

Introduction

The joining of solid metals with molten solders or filler metals involves wetting of the solid by the liquid, during which, the solid dissolves into the liquid phase, and/or an intermetallic phase or phases form between the spreading liquid and the solid substrate. The strength of the joint depends on many factors such as wettability, solubility, and properties of the formed intermetallic compound (see Boettinger et al. (1993) and Eustathopoulos et al. (1999) for general discussion).

The mechanisms of reactive wetting involve the interplay of fluid flow, heat and mass transport, capillary phenomena, and phase transformations. To our knowledge, a comprehensive model that incorporates all these effects is still non-existent. Previous attempts to model reactive wetting in high-temperature metallic systems involved fitting experimental dynamic contact angle or base radius curves by different functions, see for example Ambrose et al. (1992, 1993); Eustathopoulos (1998); Kim et al. (2008); Dezellus et al. (2003). The empirical formula provides an easy and straightforward calculation of extent of spreading or general shape of the drop at any given time. However, these formulas does not give much insights into the mechanisms involved in the reactive spreading process, i.e., intermetallic formation. In addition, detailed study of certain effects such as phase change and dissolution can not be discerned from these formulas. On the other hand, the use of comprehensive models requires a more involved numerical calculation and can present some numerical instabilities aside from limitations in parameter ranges and choice of length and time scales.

A different analysis on the kinetics of reactive wetting has been proposed by Saiz et al. (2000). They argued that the substrate cannot be described as rigid and insoluble and with a sufficient nucleation barrier, a time regime exist in which intermetallic formation lags the liquid front. In this regime, the contact angles are then dictated by adsorption, and the spreading kinetics are controlled by the movement of a ridge formed at the liquid-solid-vapor (L-S-V) triple junction. Although, this step can happen only in the early stages of the spreading process, it can play a critical role in the succeeding steps and they proposed that it should be taken into account when modeling a specific system.

Our goal in this paper is to present a diffuse-interface model of reactive wetting with intermetallic formation. The multiphase and multicomponent approach is similar to previous work on the modeling of dissolutive wetting, see Villanueva et al. (2008, 2009). The model incorporates fluid flow, phase change, and solute diffusion. In the next section, the mathematical model and input parameters are presented, followed by a brief discussion

of the numerical approach. In the results and discussion section, we first present results for a base set of parameters. Then we focus on the factors that can affect the nucleation and growth of the intermetallic phase such as interface energies between the intermetallic and liquid, and kinetic coefficient of the intermetallic phase. Next, flow patterns and concentration profiles are discussed.

Mathematical Model and Parameters

A ternary system of substitutional elements A, B, and C with four phases, spreading liquid (denoted by L or sometimes 1 for convenience), solid substrate (S or 2), intermetallic (I or 3), and vapor (V or 4) is considered. We begin by setting the total molar Gibbs energy G given by

$$G = \int_{\Omega} \left(\frac{G_m(x_A, x_B, x_C, \phi_L, \phi_S, \phi_I, \phi_V, T)}{V_m} \right.$$
$$\left. + \sum_{i,j>i}^{4} \frac{\epsilon_{ij}^2}{2} |\phi_i \nabla \phi_j - \phi_j \nabla \phi_i|^2 \right) d\Omega , \quad (1)$$

where T is temperature, V_m is the molar volume, and $x_{A,B,C}$ are the mole fractions of A, B, C-atoms with $x_A + x_B + x_C = 1$. The phase-field variables ϕ_i's vary smoothly between 0 and 1 and we set the condition that $\phi_L + \phi_S + \phi_I + \phi_V = 1$. Our approach is similar to Villanueva et al. (2008) with the main difference of the gradient energies following an anti-symmetric form. The molar Gibbs energy is postulated as,

$$G_m = \sum_{i}^{4} P(\phi_i) G_m^i + \sum_{i,j>i}^{4} W_{ij} \phi_i^2 \phi_j^2$$
$$+ \sum_{i,j,k>j>i}^{4} W_{ijk} \phi_i^2 \phi_j^2 \phi_k^2 + W_{LSIV} \phi_L^2 \phi_S^2 \phi_I^2 \phi_V^2, \quad (2)$$

with the smoothed step function $P(\phi_i) = \phi_i^3(10 - 15\phi_i + 6\phi_i^2)$. The coefficients ϵ_{ij}'s and W's are related to the thicknesses and interfacial energies. An ideal solution for $G_m^{L,S,V}$ and a regular solution for G_m^I are assumed, and they take the form

$$G_m^i = x_A {}^o G_A^i + x_B {}^o G_B^i + (1 - x_A - x_B) {}^o G_C^i$$
$$+ RT(x_A \ln x_A + x_B \ln x_B + (1 - x_A - x_B) \cdot$$
$$\ln(1 - x_A - x_B)), \quad i = L, S, V, \quad (3)$$

and

$$G_m^I = x_A {}^o G_A^I + x_B {}^o G_B^I + (1 - x_A - x_B) {}^o G_C^I$$
$$+ RT(x_A \ln x_A + x_B \ln x_B + (1 - x_A - x_B) \cdot$$
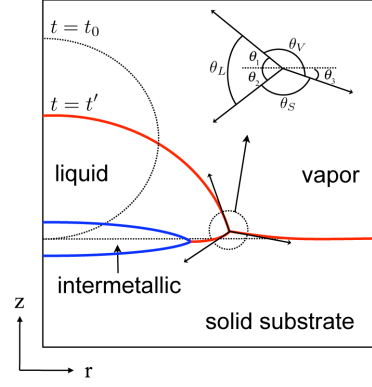$$\ln(1 - x_A - x_B)) + \Omega x_A x_B, \quad (4)$$

Figure 1: Schematic diagram of a reactive wetting with intermetallic formation.

where, for example, ${}^o G_A^L$ is the molar Gibbs energy of pure A in the liquid phase and R is the gas constant.

An isothermal, viscous, and incompressible system is considered. The governing equations, similar to our approach in Villanueva et al. (2008) and Villanueva et al. (2009), are the following:

(i) conservative convective concentration equations,

$$\frac{1}{V_m} \left(\frac{\partial x_A}{\partial t} + \mathbf{u} \cdot \nabla x_A \right) = -\nabla \cdot J_A \quad \text{and} \quad (5)$$

$$\frac{1}{V_m} \left(\frac{\partial x_B}{\partial t} + \mathbf{u} \cdot \nabla x_B \right) = -\nabla \cdot J_B, \quad (6)$$

where $\mathbf{u}$ is the flow velocity and J_A and J_B are fluxes of A and B measured with respect to the local flow,

(ii) non-conservative convective Allen-Cahn equations for the phase-field variables,

$$\frac{\partial \phi_i}{\partial t} + \mathbf{u} \cdot \nabla \phi_i = -M_{\phi_i} \frac{\delta G}{\delta \phi_i}, \quad i = L, S, I, \quad (7)$$

where M_{ϕ_i}'s are kinetic mobilities and with natural boundary conditions $\mathbf{n} \cdot \nabla \phi_i = 0$,

(iii) a mass continuity equation for incompressible flow,

$$\nabla \cdot \mathbf{u} = 0 \quad (8)$$

(iv) and the Navier-Stokes equations for incompressible flow with added surface tension forces,

$$\rho(\phi) \left(\frac{\partial \mathbf{u}}{\partial t} + \mathbf{u} \cdot \nabla u \right) = -\nabla \tilde{p} + \nabla \cdot \mu(\phi)(\nabla \mathbf{u} + \nabla \mathbf{u}^T)$$
$$- \sum_{i=L,S,I} \phi_i \nabla \left(\frac{\delta G}{\delta \phi_i} \right), \quad (9)$$

where $\tilde{p}$ is a nonclassical pressure.

2

To complete the concentration equations (Eqns. 5-6), we write the interdiffusion flux of solutes J_A and J_B (with $J_A + J_B + J_C = 0$)

$$J_A = -L_{AA}\nabla\left(\frac{\delta G}{\delta x_A}\right) - L_{AB}\nabla\left(\frac{\delta G}{\delta x_B}\right) \quad \text{and} \quad (10)$$

$$J_B = -L_{AB}\nabla\left(\frac{\delta G}{\delta x_A}\right) - L_{BB}\nabla\left(\frac{\delta G}{\delta x_B}\right), \quad (11)$$

where the variation in G with respect to the compositions x_j are given by

$$\frac{\delta G}{\delta x_j} = \frac{1}{V_m}\frac{\partial G_m}{\partial x_j}, \quad j = A, B, \quad (12)$$

and the L_{ij}'s are

$$\begin{aligned} L_{AA} &= (1 - x_A)^2 x_A M_A(\phi_L, \phi_S, \phi_I, \phi_V) \\ &+ x_A^2 x_B M_B(\phi_L, \phi_S, \phi_I, \phi_V) \\ &+ x_A^2 (1 - x_A - x_B) M_C(\phi_L, \phi_S, \phi_I, \phi_V), \quad (13) \end{aligned}$$

$$\begin{aligned} L_{BB} &= x_B^2 x_A M_A(\phi_L, \phi_S, \phi_I, \phi_V) \\ &+ (1 - x_B)^2 x_B M_B(\phi_L, \phi_S, \phi_I, \phi_V) \\ &+ x_B^2 (1 - x_A - x_B) M_C(\phi_L, \phi_S, \phi_I, \phi_V), \quad \text{and} \\ & \quad (14) \end{aligned}$$

$$\begin{aligned} L_{AB} &= -(1 - x_A) x_A x_B M_A(\phi_L, \phi_S, \phi_I, \phi_V) \\ &- x_A x_B (1 - x_B) M_B(\phi_L, \phi_S, \phi_I, \phi_V) \\ &+ x_A (1 - x_A - x_B) x_B M_C(\phi_L, \phi_S, \phi_I, \phi_V). \\ & \quad (15) \end{aligned}$$

The mobilities of A, B, and C can be different in each phase and are given by

$$\begin{aligned} M_j(\phi_L, \phi_S, \phi_I, \phi_V) &= M_j^L \phi_L + M_j^S \phi_S + M_j^I \phi_I \\ &+ M_j^V (1 - \phi_L - \phi_S - \phi_I), \quad j = A, B, C, \quad (16) \end{aligned}$$

where $1 - \phi_L - \phi_S - \phi_I$ has been substituted for ϕ_V. In the interior of the phases, the diffusivities, D_{ij}, are defined through the expressions,

$$J_A = -\frac{D_{AA}}{V_m}\nabla x_A - \frac{D_{AB}}{V_m}\nabla x_B \quad \text{and} \quad (17)$$

$$J_B = -\frac{D_{BA}}{V_m}\nabla x_A - \frac{D_{BB}}{V_m}\nabla x_B. \quad (18)$$

Input Parameters. The model allows for a ternary phase diagram such as the one shown as an isothermal section in Figure 2. The phase diagram is idealized and the parameters are given in Table 1 along with other input parameters.

Given the parameters in Table 1, we can estimate more familiar material parameters such as diffusivities D_i, and interface kinetic coefficients k_{coeff} with the following formulas (Boettinger et al. (2002)),

$$D_L = M_x^L RT, \quad \text{etc.} \quad (19)$$

$$k_{\text{coeff}} = \frac{V_m}{3RM_\phi\delta} \quad (20)$$

Table 1: Base set of parameters.

$^oG_A^L = -5.0 \times 10^3 \; \frac{\text{J}}{\text{mol}}$
$^oG_B^L = {}^oG_C^L = {}^oG_C^S = {}^oG_C^S = {}^oG_C^I$
$\quad = -1/2 \cdot {}^oG_A^L$
$^oG_B^S = {}^oG_A^I = 1/4 \cdot {}^oG_A^L$
$^oG_B^I = -1/8 \cdot {}^oG_A^L$
$^oG_A^V = -{}^oG_A^L$
$^oG_B^V = -2 \cdot {}^oG_A^L$
$^oG_C^V = 1/2 \cdot {}^oG_A^L$
$\Omega_{AB} = 5/4 \cdot {}^oG_A^L$
$M_A^L = M_B^L = M_C^L = M_A^V = M_B^V = M_C^V$
$\quad = 2.67 \times 10^{-13} \; \frac{\text{mol m}^2}{\text{Js}}$
$M_A^S = M_B^S = M_C^S = M_A^I = M_B^I = M_C^I$
$\quad = 10^{-3} \cdot M_A^L$
$\mu_L = 4.0 \times 10^{-3} \; \text{Pa} \cdot \text{s}$
$\mu_S = \mu_I = 10^6 \cdot \mu_L$
$\mu_V = 10^{-2} \cdot \mu_L$
$\rho_L = 10^3 \; \frac{\text{kg}}{\text{m}^3}$
$\rho_S = \rho_I = 1.05 \cdot \rho_L$
$\rho_V = 10^{-3} \cdot \rho_L$
$M_{\phi_L} = M_{\phi_S} = M_{\phi_I} = 25 \; \frac{\text{m}^3}{\text{Js}}$
$T = 450 \; \text{K}$
$W_{LS} = 2.21 \times 10^5 \; \frac{\text{J}}{\text{mol}}$
$W_{LI} = 1.91 \times 10^4 \; \frac{\text{J}}{\text{mol}}$
$W_{LV} = 1.43 \times 10^5 \; \frac{\text{J}}{\text{mol}}$
$W_{SI} = 2.54 \times 10^4 \; \frac{\text{J}}{\text{mol}}$
$W_{SV} = 2.49 \times 10^5 \; \frac{\text{J}}{\text{mol}}$
$W_{IV} = 2.33 \times 10^5 \; \frac{\text{J}}{\text{mol}}$
$W_{ijk} = W_{LSIV} = 8.75 \times 10^6 \; \frac{\text{J}}{\text{mol}}$
$\epsilon_{LS}^2 = 6.32 \times 10^{-9} \; \frac{\text{J}}{\text{m}}$
$\epsilon_{LI}^2 = 6.71 \times 10^{-10} \; \frac{\text{J}}{\text{m}}$
$\epsilon_{SI}^2 = 7.40 \times 10^{-10} \; \frac{\text{J}}{\text{m}}$
$\epsilon_{LV}^2 = 5.99 \times 10^{-9} \; \frac{\text{J}}{\text{m}}$
$\epsilon_{SV}^2 = 8.24 \times 10^{-9} \; \frac{\text{J}}{\text{m}}$
$\epsilon_{IV}^2 = 7.94 \times 10^{-9} \; \frac{\text{J}}{\text{m}}$
$V_M = 1.0 \times 10^{-5} \; \frac{\text{m}^3}{\text{mol}}$
$R = 8.31 \; \frac{\text{J}}{\text{mol K}}$

Table 2: Calculated interface energies γ_{ij}'s.

$^*\gamma_{LS} = 2.55 \; \frac{\text{J}}{\text{m}^2}$	$\gamma_{LV} = 1.91 \; \frac{\text{J}}{\text{m}^2}$	$\gamma_{SV} = 2.17 \; \frac{\text{J}}{\text{m}^2}$
$\gamma_{LI} = 0.29 \; \frac{\text{J}}{\text{m}^2}$	$\gamma_{SI} = 0.35 \; \frac{\text{J}}{\text{m}^2}$	$\gamma_{IV} = 1.99 \; \frac{\text{J}}{\text{m}^2}$

*Since the liquid-solid interface is unstable with the given base set of parameters, the liquid-solid interface energy is calculated by suppressing the formation of the intermetallic phase.

Table 3: Recalculated interface energies γ_{ij}'s with $W_{LI} = 1.47 \times 10^5 \; \frac{\text{J}}{\text{mol}}$ and $\epsilon_{LI}^2 = 3.87 \times 10^{-9} \; \frac{\text{J}}{\text{m}}$ while keeping the rest of the parameters the same.

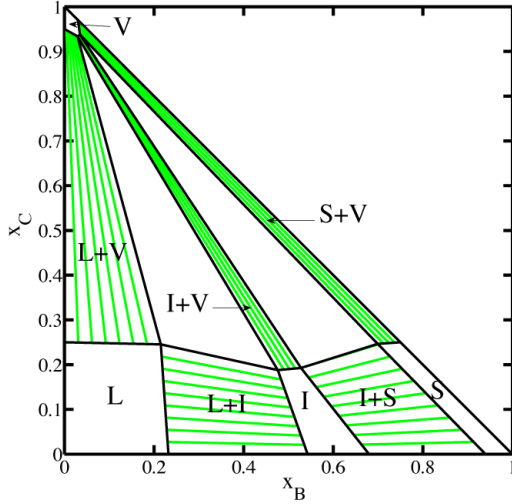|		
$\gamma_{LS} = 2.55 \; \frac{\text{J}}{\text{m}^2}$	$\gamma_{LV} = 1.93 \; \frac{\text{J}}{\text{m}^2}$	$\gamma_{SV} = 2.17 \; \frac{\text{J}}{\text{m}^2}$
$\gamma_{LI} = 1.54 \; \frac{\text{J}}{\text{m}^2}$	$\gamma_{SI} = 0.34 \; \frac{\text{J}}{\text{m}^2}$	$\gamma_{IV} = 2.03 \; \frac{\text{J}}{\text{m}^2}$

Figure 2: Idealized phase diagram of a ternary A-B-C system at 450 K with four phases; liquid (L), solid (S), intermetallic (I), and vapor (V).

where $M_x^i = M_A^i = M_B^i = M_C^i$, $i = L, S, I, V$. The diffusivities are $D_L = 10^{-9} \frac{m^2}{s}$, $D_S = 10^{-12} \frac{m^2}{s}$, and $D_I = 10^{-12} \frac{m^2}{s}$ while the kinetic coefficients are $k_{coeff}^i = 16 \frac{sK}{m}$ where $i = L, S, I$.

Interface energies. Exact values for the interface energies were obtained from 1D simulations of each pair of phases (LS, LI, LV, SI, SV, and IV). The interface energies are computed from the expression,

$$\gamma = \int_{-\infty}^{\infty} \left[\frac{1}{V_m} \left((G_m(x_i(z), \phi_i(z); T) \right. \right.$$
$$- G_m(x_i(\pm\infty), \phi_i(\pm\infty); T))$$
$$\left. - \sum_{i=1}^{2} \frac{\partial G_m(x_i, \phi_i; T)}{\partial x_i} \right|_{z=\pm\infty} \cdot (x_i(z) - x_i(\pm\infty)) \right)$$
$$+ \sum_{i,j>i}^{4} \frac{\epsilon_{ij}^2}{2} |\phi_i \nabla \phi_j - \phi_j \nabla \phi_i|^2 \right] dz, \tag{21}$$

and the values are summarized in Table 2.

Numerical Approach

The numerical simulations were carried out using Fem-Lego (Amberg et al. (1999)), an open source PDE solver with mesh adaptive finite element method. All PDEs are discretized in space using piecewise linear functions. Each resulting linear systems are solved using Krylov-type iteration methods either by the conjugate gradient method (CG) for symmetric and positive-definite systems or the generalized minimal residual method (GM-RES) otherwise. The system of Navier-Stokes equa-
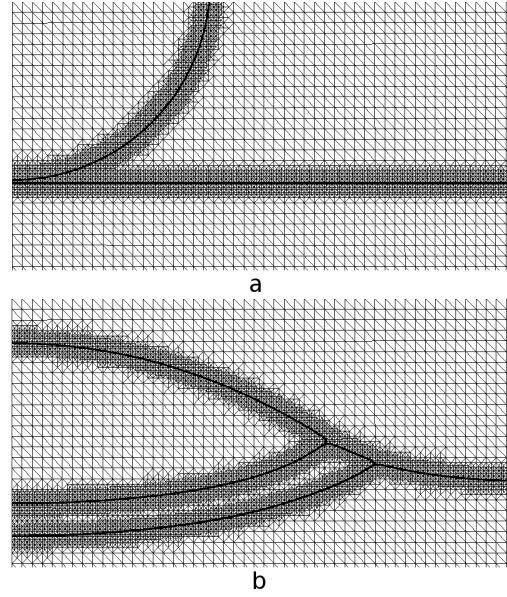

Figure 3: Adaptive mesh refinement and derefinement of cut-off regions corresponding to two different times with superimposed 0.5 contours of the phase-field variables ϕ_L, ϕ_S, and ϕ_I.

tions and continuity equation is solved by an incremental fractional-step algorithm (Guermond and Quartapelle (1998)) that belongs to a class of projection methods. A pressure stabilization term is also added in the projection step to improve stability.

Adaptive mesh refinement and derefinement is utilized due to the need to spatially resolve the interfaces as a consequence of the phase-field approach. In Figure 3, cut-off regions corresponding to two different times (initial and late stage spreading) are shown illustrating the effective implementation of the mesh refinement and derefinement. An *ad hoc* error criterion is used to ensure mesh resolution along the vicinity of the interfaces. See Do-Quang et al. (2007) for details of the mesh adaptive finite element scheme. For the typical example shown in Figure 3, the initial radius of the drop is $R_0 = 20$ nm and the domain size is (60 nm $\times$ 90 nm). The minimum mesh size is $h_{min} = 0.13$ nm with nodes between 9000-11000 and triangular elements between 19000-22000. The capillary time scale $t_c = \mu_L R_0 / (2\gamma_{LV})$ is considered in this study to be especially important which represents the natural response of the system to reach mechanical equilibrium.

Results and Discussion

Results with a base set of parameters given in Table 1 are first presented. The initial configuration is a drop that
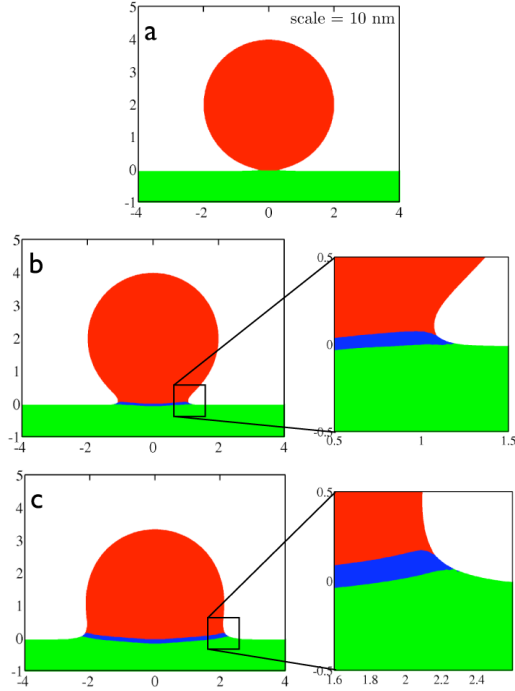
4

Figure 4: Numerical simulation of the spreading of a molten metal drop on a solid substrate with the formation of intermetallic phase between the drop and the substrate. The figure shows snapshots with a maximum phase-field plot at times $t/t_c = 0, 1, 200$ where t_c is a capillary time scale.

barely touches the substrate with a contact angle close to 180°, see Figure 4a. There are two ways to visualize the configuration. Either the 0.5 contours of the phase-field variables or the maximum phase-field as shown in Figure 4 can be plotted, that is, at every discrete point in the domain we find the phase-field variable that has the maximum value and then designate a corresponding color; red for ϕ_1, green for ϕ_2, blue for ϕ_3, and white for ϕ_4. The maximum phase-field plot has been chosen since it can directly identify triple junctions, which facilitates the measurement of contact angles following our previous approach in Villanueva et al. (2009).

The early stage of spreading is always rapid as viscous or inertial forces dominate followed by a slow and progressive spreading as diffusion becomes the dominant process. However, phase change can also affect the spreading process in both stages as it was found in Villanueva et al. (2009) for dissolutive wetting. Figure 4b shows an early time $t/t_c = 1$ where the base radius has increased to $R/R_0 = 1.07$ with an apparent contact angle of the drop at 132.3^o. The growth of the intermetallic phase is also rapid, as expected by a balance of tensions with the set of interface energies in Table 2. In the
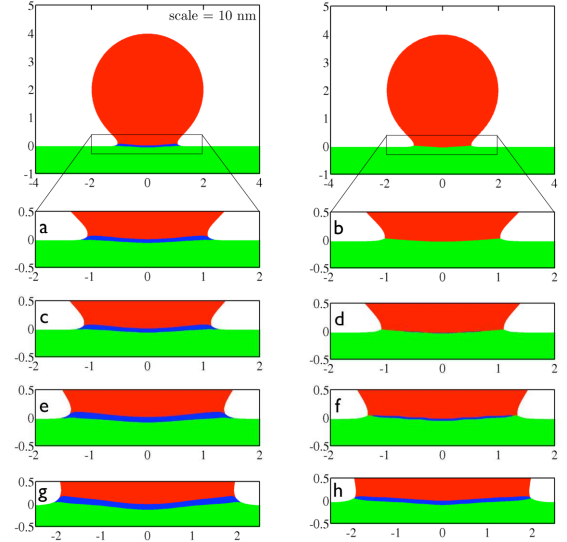

Figure 5: Comparison of the growth of intermetallic phase between a fast intermetallic kinetics (a-c-e-g) corresponding to times $t/t_c = 1, 1.3, 3, 20$, respectively, and a slow intermetallic kinetics (b-d-f-g) with the same corresponding times, respectively. In both cases the intermetallic phase eventually grows ahead of the spreading liquid drop.

magnified view of Figure 4b, we see that the intermetallic phase has grown ahead of the spreading liquid and forms LIV and SIV triple junctions. The drop profile including the structure of the contact line region is qualitatively similar to SEM images of a Sn-0.7 Cu solder on a Cu-substrate performed experimentally by Nogita et al. (2009). The drop continues to spread further and reaches $R/R_0 = 2.14$ at time $t/t_c = 200$ as shown in Figure 4c. While the intermetallic phase thickens but remain ahead of the spreading liquid. In the magnified view of the contact line region, one can observe that the solid substrate is not planar, nor is the intermetallic layer which is consistent with SEM images of contact line regions reported in the literature, e.g. Yin et al. (2008) and Nogita et al. (2009).

Note that there are four possible triple junctions that can be formed, namely, LSV, LIV, SIV, and LIS. Only two stable triple junctions (LIV and SIV) are formed given the set of interface energies in Table 2. In principle there should be a case where the other two triple junctions, LSV and LIS, are stable and co-exist. In this case the intermetallic phase remains behind the spreading liquid until equilibrium. However we have yet to find the set of interface energies that will give this outcome. In addition, there is the possibility of forming a stable LSIV quadrijunction as proposed by Cahn & Van Vleck (1999) but it is a challenge to find the set of interface
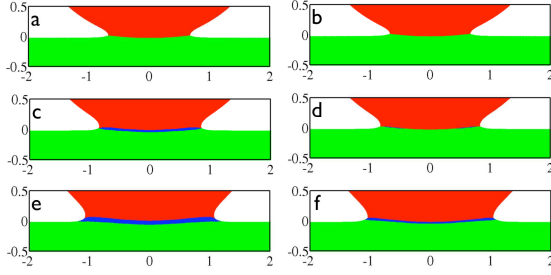
Figure 6: Comparison of the growth of intermetallic phase with different liquid-intermetallic interface energies: (a-c-e) $\gamma_{LI} = 0.29 \frac{J}{m^2}$ at times $t/t_c = 0.1, 0.3, 1.0$, respectively, and (b-d-f) $\gamma_{LI} = 1.54 \frac{J}{m^2}$ at times $t/t_c = 0.1, 0.3, 1.0$, respectively.

energies that will generate this particular case given our present methodology.

A number of factors can affect the nucleation and growth of the intermetallic phase such as interface energies between the intermetallic and other phases, and kinetic coefficients of the intermetallic phase. The present phase field model does not cleanly separate the equivalent interface kinetic coefficients for the LI and SI interfaces. However by decreasing the mobility of the phase field for the intermetallic phase, one can retard the growth of the intermetallic between the liquid and solid phases. Using the approximate formular in Equation 19, a case is now considered where the mobility of the phase field is lowered by a factor of 12 from the base state, while leaving the rest of the parameters the same. The intermetallic phase becomes more sluggish in the sense that it will respond more slowly to disequilibrium. In Figure 5, a comparison between the two cases, fast intermetallic kinetics (which corresponds to 16 sK/m) and slow intermetallic kinetics (192 sK/m) is shown. Figures 5a-c-e-g show snapshots for the fast kinetics case with a sequence in time, $t/t_c = 1, 1.3, 3, 20$, respectively, while Figures 5b-d-f-g correspond to the slow kinetics case with the same time sequence, respectively. At $t/t_c = 1$, the intermetallic phase has grown ahead of the liquid drop with the fast kinetics case (Figure 5a) while no intermetallic phase has yet grown between the liquid drop and the substrate with the slow kinetics case (Figure 5b). The base radii of the liquid drop for both cases are essentially identical at $R/R_0 = 1.07$ for the fast kinetics case and $R/R_0 = 1.03$ for the slow kinetics case. The apparent contact angles θ_1 for both cases are less than a degree apart, 132.3^o for the fast kinetics case while 132.1^o for the slow kinetics case. The time sequence $t/t_c = 1.3, 3, 20$ for the fast kinetics case (Figure 5c-e-g) shows the intermetallic phase moves together but always ahead of the liquid drop. The thick-
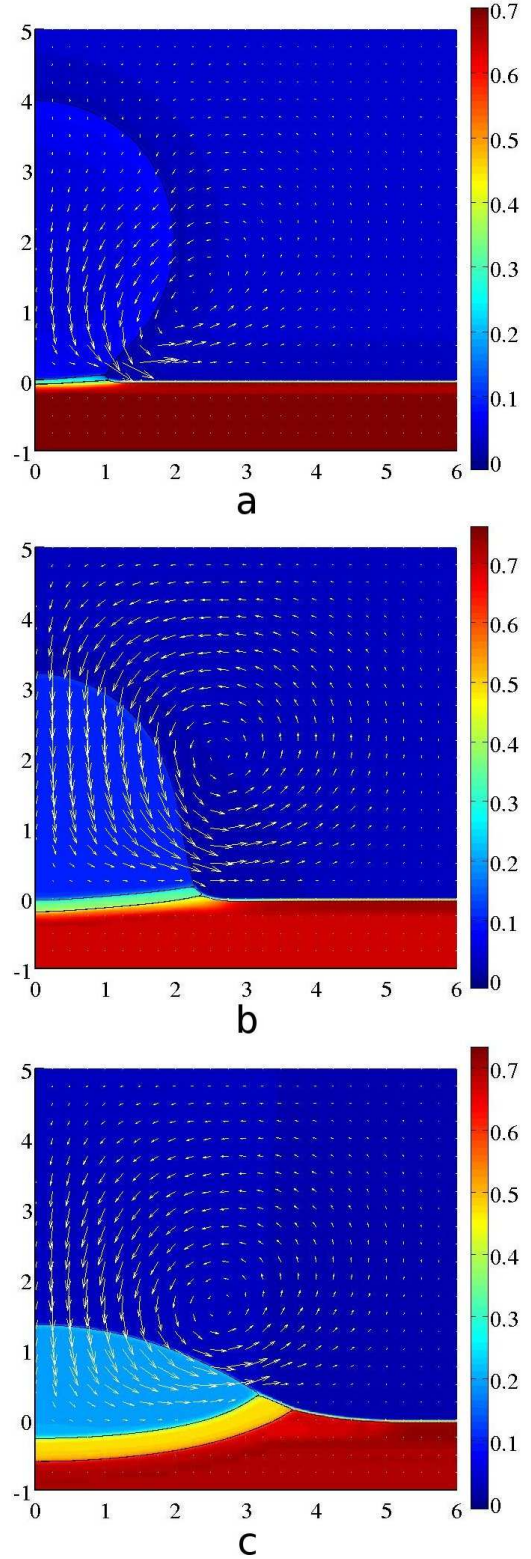

Figure 7: Concentration profiles of B at (a) early fast-spreading stage $t/t_c = 1$, (b) intermediate stage $t/t_c = 20$, and (c) late slow-spreading stage $t/t_c = 200$ with superimposed normalized velocity profiles and 0.5 contours of the phase-field variables ϕ_L, ϕ_S, and ϕ_I.

ness of the intermetallic phase is also increasing while it slowly penetrates the substrate. The intermetallic phase is non-planar and so is the substrate. The time sequence $t/t_c = 1.3, 3, 20$ for the slow kinetics case (Figure 5d-f-h) shows the nucleation and growth of the intermetallic phase. The base radii of the liquid drops compared to the same corresponding snapshot in the fast kinetics case are also less than an interface thickness in difference. While the contact angles are less than a degree in difference except for the time $t/t_c = 20$ where the fast kinetics case is 2.4^o lower in θ_1.

Figure 6 shows the effect of increasing the liquid-intermetallic interface energy γ_{LI} from $0.29 \frac{J}{m^2}$ to $1.54 \frac{J}{m^2}$ on the nucleation and growth of the intermetallic phase. We should note that varying an interface energy γ_{ij} in the model means modifying the corresponding parameter W_{ij} and ϵ_{ij} which can also alter the other interface energies. However, a 1D recalculation of the interface energies with the changes in the LI-interface, $W_{LI} = 1.47 \times 10^5 \frac{J}{mol}$ and $\epsilon_{LI}^2 = 3.87 \times 10^{-9} \frac{J}{m}$ (while keeping the rest of the parameters the same), yielded a slight change in other interface energies (see Table 3).

Snapshots for $\gamma_{LI} = 0.29 \frac{J}{m^2}$ at times $t/t_c = 0.1, 0.3, 1.0$ are shown in Figures 6a-c-e, respectively, while Figures 6b-d-f correspond to $\gamma_{LI} = 1.54 \frac{J}{m^2}$ with the same time sequence, respectively. At $t/t_c = 0.1$ in Figures 6a and 6b, both cases has no intermetallic growth and the profiles are almost identical. But then at $t/t_c = 0.3$, the growth of the intermetallic phase with $\gamma_{LI} = 0.29 \frac{J}{m^2}$ (Figure 6c) has become noticeable as compared to the case with a higher $\gamma_{LI} = 1.54 \frac{J}{m^2}$ (Figure 6d) where the intermetallic phase has just about to nucleate. At a later time $t/t_c = 1.0$ with the lower γ_{LI} (Figure 6e), the intermetallic phase grows thicker and is now clearly ahead of the spreading liquid. While the case with a higher γ_{LI} (Figure 6f), the growth of the intermetallic phase has become noticeable but it is thinner compared to the case with lower γ_{LI}. Thus Figure 6 demonstrates that a higher liquid-intermetallic interface energy can also retard the growth of the intermetallic phase although the intermetallic phase finally gets ahead of the spreading liquid.

The initial concentrations in each phases can be set arbitrarily in the model. At equilibrium, the liquid phase is rich in A while the substrate is rich in B (refer to the phase diagram in Figure 2). Initially, we start with the substrate having equilibrium values of $x_A^S = 0.05$ and $x_B^S = 0.70$ while the liquid has lower concentration of B, $x_B = 0.05$, than the equilibrium value of $x_B = 0.22$ but higher concentration of A, $x_A = 0.85$, than the equilibrium value of $x_A^L = 0.54$. Solute diffusion is much slower than fluid flow. So for the purpose of demonstrating that the concentrations in the liquid and intermetallic reaches their corresponding stable or equilibrium val-

ues within a feasible computational time frame (see Figure 7), we increase the effect of diffusion compared to fluid flow, that is, the ratio between the solute transport due to convection and solute transport due to diffusion (also known as solutal Peclet number) is decreased by a factor of 500. Figure 7a shows the concentration profile of B at an early spreading stage $t/t_c = 1$ with a superimposed normalized velocity profile and 0.5 contours of the phase-field variables ϕ_L, ϕ_S, and ϕ_I. The concentration of B in the liquid evaluated at the center of the drop (along the z-axis and midpoint between the LV and LI-interface) has only increased by $2 \cdot 10^{-5}$ from the initial value of $x_B = 0.05$ while the concentration of A (not shown) has increased by $3 \cdot 10^{-4}$ from the initial value of $x_A = 0.85$. The intermetallic phase has formed at this time and has spread ahead of the liquid phase. The flow pattern consists of a vortex with center outside of the drop and near the liquid-vapor interface, and a flow downward from the upper part of the drop then redirected to the contact line region. And as expected, there is negligible flow in the solid substrate and in the intermetallic phase at any given time. The base radius of the liquid drop is $R/R_0 = 1.07$ and has a contact angle $\theta_L = 137.6^o$.

At an intermediate stage $t/t_c = 20$ (Figure 7b), the drop spread further with a base radius $R/R_0 = 2.30$ and a contact angle $\theta_L = 85.4^o$. The flow pattern is generally the same compared to the previous time $t/t_c = 1$ except that the vortex moves further away from the solid substrate. The concentration of A and B in the liquid are $x_A = 0.73$ and $x_B = 0.10$, respectively. While the concentrations in the intermetallic phase are $x_A = 0.44$ and $x_B = 0.37$. Since the average concentration of the system implies only three-phase SIV co-existence, the liquid drop is expected to disappear at equilibrium. In addition, the equilibrium concentration of the intermetallic phase is expected to reach the I-corner of the SIV co-existence triangle (see phase diagram) which has values $x_A^I = 0.28$ and $x_B^I = 0.53$. At a later stage $t/t_c = 200$ (Figure 7c), the liquid drop shrank, the intermetallic phase expanded, and portion of the substrate has dissolved. Furthermore, the liquid drop has spread further with $R/R_0 = 3.24$ and contact angle $\theta_L = 61.2^o$. The concentration of A and B in the liquid are $x_A = 0.60$ and $x_B = 0.20$, respectively, and are close to the stable values $x_A = 0.54$ and $x_B = 0.22$ (that corresponds to the L-corner of the LIV co-existence triangle in the phase diagram). The concentration of A and B of the intermetallic layer are $x_A = 0.36$ and $x_B = 0.48$ with its source of A-atoms coming from the liquid drop and B-atoms from the substrate. Although the average concentration ($\tilde{x}_A = 0.07, \tilde{x}_B = 0.35$) lies inside the SIV co-existence triangle, these concentrations are closer to the I-corner of the LIV co-existence triangle, that has

values $x_A = 0.34$ and $x_B = 0.48$, than the I-corner of the SIV co-existence triangle that has values $x_A = 0.28$ and $x_B = 0.53$. A check at times $t/tc = 300, 400, 500$ yielded the values $(x_A = 0.36, x_B = 0.48), (x_A = 0.36, x_B = 0.48), (x_A = 0.36, x_B = 0.47)$ respectively, which are also closer to the I-corner of the LIV co-existence triangle. However, a validation by examining planar interface (1D) confirms that a three phase SIV co-existence yields the right concentrations at the corners of the SIV co-existence triangle.

Conclusions

We have presented a multicomponent and multiphase model of reactive wetting with intermetallic formation. The model incorporates fluid flow, phase change, and solute diffusion. Numerical simulations were performed successfully revealing the complex behavior of the reactive wetting process that include the nucleation and growth of an intermetallic phase, initial rapid spreading followed by a slow and progressive spreading. In addition, we have shown that the formation of the intermetallic phase can be controlled by the kinetic coefficient of the intermetallic phase and/or interface energy associated with it.

References

Amberg G., Tönhardt R., and Winkler C., Finite element simulations using symbolic computing, Math. & Comp. in Sim., Vol. 49, 257-274, 1999

Ambrose J.C., Nicholas M.G., Stoneham A.M., Dynamics of braze spreading, Acta Metall. Mater., Vol. 40, 2483-2488, 1992

Ambrose J.C., Nicholas M.G., Stoneham A.M., Dynamics of liquid drop spreading in metal-metal systems, Acta Metall. Mater., Vol. 41, 2395-2401, 1993

Boettinger W.J., Handwerker C.A., Kattner U.R., Reactive wetting and intermetallic formation, In: Frear D., Hosking F.M. Yost F., editors, The mechanics of solder alloy wetting and spreading, New York: Van Nostrand Reinhold, Chapter 4, 103-139, 1993

Boettinger W.J., Warren J.A., Beckermann C., Karma A., Phase-field simulation of solidification, Ann. Rev. Mater. Res., Vol. 32, 163-194, 2002

Cahn J.W., Van Vleck E.S., On the co-existence and stability of trijunctions and quadrijunctions in a simple model, Acta Mater., Vol. 47, 4627-4639, 1999

Dezellus O., Hodaj F., Eustathopoulos N., Progress in modelling of chemical-reaction limited wetting, J. Eur. Ceram. Soc., Vol. 23, 2797-2803, 2003

Do-Quang M., Villanueva W., Singer-Loginova I., and Amberg G., Parallel adaptive computation of some time-dependent materials-related microstructural problems, Bull. Pol. Acad. Sci., Vol. 55, 229-237, 2007

Eustathopoulos N., Dynamics of wetting in reactive metal/ceramic systems, Acta Mater., Vol. 46, 2319-2327, 1998

Eustathopoulos N., Nicholas M.G., Drevet B., Wettability at high temperatures, Pergamon Materials Series, Elsevier, Amsterdam, 1999

Guermond J.L. and Quartapelle L., On stability and convergence of projection methods based on pressure Poisson equation, Int. J. Numer. Methods Fluids, Vol. 26, 1039-1053, 1998

Kim C., Kang S.C., Baldwin D.F., Experimental evaluation of wetting dynamics models for $Sn_{63}Pb_{37}$ and $SnAg_{4.0}Cu_{0.5}$ solder materials, J. Appl. Phys., Vol. 104, 033537, 2008

Nogita K., Gourlay C.M., Nishimura T., Cracking and phase stability in reaction layers between Sn-Cu-Ni solders and Cu substrates, JOM, Vol. 61, 45-51, 2009

Saiz E., Cannon R.M., Tomsia A.P., Reactive spreading: adsorption, ridging and compound formation, Acta Mater., Vol. 48, 4449-4462, 2000

Villanueva W., Grönhagen K., Amberg G., and Ågren J., Multicomponent and multiphase modeling and simulation of reactive wetting, Phys. Rev. E, Vol. 77, 056313, 2008

Villanueva W., Boettinger W.J., Warren J.A., and Amberg G., Effect of phase change and solute diffusion on spreading on a dissolving substrate, Acta Mater., Vol. 57, 6022-6036, 2009

Yin L., Chauhan A., Singler T.J., Reactive wetting in metal/metal systems: Dissolutive versus compound-forming systems, Mat. Sci. Engng-A, Vol. 495, 80-89, 2008